Front. Chem. Sci. Eng. 2021, 15(6): 1561–1571
https://doi.org/10.1007/s11705-021-2089-z

RESEARCH ARTICLE

Superior performance in visible-light-driven hydrogen evolution reaction of three-dimensionally ordered macroporous $SrTiO_3$ decorated with $Zn_xCd_{1-x}S$

Huiying Quan[1], Kejiang Qian[2], Ying Xuan[1], Lan-Lan Lou[2], Kai Yu (✉)[1], Shuangxi Liu[2]

1 MOE Key Laboratory of Pollution Processes and Environmental Criteria, Tianjin Key Laboratory of Environmental Technology for Complex Transmedia Pollution, College of Environmental Science and Engineering, Nankai University, Tianjin 300350, China
2 Institute of New Catalytic Materials Science and MOE Key Laboratory of Advanced Energy Materials Chemistry, School of Materials Science and Engineering, National Institute of Advanced Materials, Nankai University, Tianjin 300350, China

Abstract It is of broad interest to develop emerging photocatalysts with excellent light-harvesting capacity and high charge carrier separation efficiency for visible light photocatalytic hydrogen evolution reaction. However, achieving satisfying hydrogen evolution efficiency under noble metal-free conditions remains challenging. In this study, we demonstrate the fabrication of three-dimensionally ordered macroporous $SrTiO_3$ decorated with $Zn_xCd_{1-x}S$ nanoparticles for hydrogen production under visible light irradiation ($\lambda > 420$ nm). Synergetic enhancement of photocatalytic activity is achieved by the slow photon effect and improved separation efficiency of photogenerated charge carriers. The obtained composites could afford very high hydrogen production efficiencies up to 19.67 $mmol \cdot g^{-1} \cdot h^{-1}$, with an apparent quantum efficiency of 35.9% at 420 nm, which is 4.2 and 23.9 times higher than those of pure $Zn_{0.5}Cd_{0.5}S$ (4.67 $mmol \cdot g^{-1} \cdot h^{-1}$) and CdS (0.82 $mmol \cdot g^{-1} \cdot h^{-1}$), respectively. In particular, under Pt-free conditions, an attractive hydrogen production rate (3.23 $mmol \cdot g^{-1} \cdot h^{-1}$) was achieved, providing a low-cost and high-efficiency strategy to produce hydrogen from water splitting. Moreover, the composites showed excellent stability, and no obvious loss in activity was observed after five cycling tests.

Keywords three-dimensionally ordered macroporous $SrTiO_3$, $Zn_xCd_{1-x}S$, visible light, hydrogen production, promotion mechanism

Received May 1, 2021; accepted July 2, 2021

E-mail: kaiyu@nankai.edu.cn

1 Introduction

The utility of solar energy to produce hydrogen by semiconductor photocatalysts has become a promising alternative to fossil fuels to reduce global warming [1]. In the past decades, considerable effort has been devoted to adjust the energy band structure [2,3], enhance the charge separation efficiency [4,5], and increase the light-harvesting capacity [6,7] of semiconductors. However, developing stable and efficient photocatalysts with wide-spectrum response remains challenging [8]. Recently, three-dimensionally ordered macroporous (3DOM) semiconductor materials with inverse opal structure have received enormous attention in the photocatalysis field due to their unique slow photon effect and extremely improved light-harvesting efficiency [9–11]. Various 3DOM semiconductors, such as WO_3 [12,13], TiO_2 [14,15], g-C_3N_4 [16], MVO_4 (M = In, Bi) [17,18], and MoP [19], were synthesized and used as photocatalysts in water splitting and photodegradation of organic contaminants.

As a typical simple cubic perovskite material, strontium titanate ($SrTiO_3$) has extensive application prospects in the photocatalysis field due to its advantages of tailorable chemical and electronic structures, high redox property, good stability, low cost, and environmental friendliness [20,21]. Recently, the 3DOM $SrTiO_3$ materials (3D-STO) with varying macropore diameters were first reported by our group [22]. This kind of photocatalyst exhibited significantly improved photocatalytic efficiency in hydrogen production [23], CO_2 photocatalytic reduction [24], and contaminant photodegradation [25]. However, pristine 3D-STO often suffer from limited spectral response ability and serious photogenerated charge carriers' recombination due to their large bandgap (ca. 3.2 eV) and excessive

structural defects, thus impeding their real application in photocatalysis field.

S-based semiconductors have been widely investigated as photocatalysts for hydrogen evolution reaction from water splitting because their suitable valence band potential and narrow bandgap endow them with wide-spectrum responsibility [26–29]. In particular, the solid solution materials $Zn_xCd_{1-x}S$, which possess adjustable electronic band structure by tuning the molar ratio of Zn/Cd [30,31], improved stability, and less toxicity compared with CdS [32], exhibited superior photocatalytic hydrogen production performance under visible light irradiation [33–35]. However, a relatively high recombination rate of photogenerated electrons and holes were observed over pristine $Zn_xCd_{1-x}S$ solid solution materials [36]. Therefore, decorating the $Zn_xCd_{1-x}S$ nanoparticles into the macropores of 3D-STO should be an efficient strategy to combine the slow photon effect of 3DOM materials and inhibit recombination of charge carriers of heterojunction structure.

In this study, $Zn_xCd_{1-x}S$ solid solution materials with different Zn/Cd ratios were synthesized through a chemical co-precipitation method in the presence of α-monothioglycerol. The obtained $Zn_xCd_{1-x}S$ nanoparticles were dispersed into the macropores of 3D-STO with a variable mass ratio to fabricate composite photocatalysts. These photocatalysts exhibited excellent hydrogen evolution rates (up to 19.67 $mmol \cdot g^{-1} \cdot h^{-1}$) and good reusability under visible light irradiation ($\lambda > 420$ nm). Notably, an attractive hydrogen evolution rate (3.23 $mmol \cdot g^{-1} \cdot h^{-1}$) can be achieved in the absence of Pt as co-catalyst. The promoted efficiency of the photocatalysts could be attributed to the synergistic effect of the slow photon effect of 3D-STO and the improved charge transfer efficiency. Thus, this study provides a promising strategy to fabricate highly efficient visible-light-driven photocatalysts for hydrogen evolution even under noble metal-free conditions.

2 Experimental

2.1 Materials

Methyl methacrylate (stabilized with 30 $mg \cdot L^{-1}$ *p*-methoxyphenol), tetrabutyl titanate [$Ti(OBu)_4$], and chloroplatinic acid hexahydrate ($H_2PtCl_6 \cdot 6H_2O$) were obtained from Aladdin. Strontium nitrate [$Sr(NO_3)_2$] and lanthanum nitrate [$La(NO_3)_2$] was purchased from Tianjin Bodi Chemical Co., Ltd. Potassium persulfate ($K_2S_2O_8$) and citric acid monohydrate ($C_6H_8O_7$) were supplied by Sinopharm Chemical Reagent Co., Ltd. Sodium sulfide hydrate ($Na_2S \cdot 9H_2O$), cadmium acetate dihydrate [$Cd(CH_3CO_2)_2 \cdot 2H_2O$], zinc acetate [$Zn(CH_3CO_2)_2$], Na_2SO_3, and α-monothioglycerol ($C_3H_8O_2S$) were obtained from Shanghai Macklin Biochemical Co., Ltd. Nafion® 117 solution (ca. 5% in a mixture of lower aliphatic alcohols and water) was purchased from Sigma-Aldrich. All chemicals were reagent grade and used as received without further purification.

2.2 Characterization

Powder X-ray diffraction (XRD) patterns were recorded on a Rigaku SmartLab X-ray diffractometer (Cu Kα radiation) with a scanning rate of $6° \cdot min^{-1}$ at 40 kV and 40 mA. The morphology, elemental mapping, and lattice fringes of the samples were observed using a JEOL JSM-7500F field-emission scanning electron microscope (SEM) and a Philips Tecnai G2 F20 field-emission transmission electron microscope (TEM) equipped with energy dispersive X-ray spectrometers (EDS). The diffuse reflection ultraviolet-visible spectra (DR UV-Vis) of samples were tested by Shimazu UV-2550 spectrometer equipped with an integrating sphere using $BaSO_4$ as a reference in the range of 200–800 nm. Brauner-Emmett-Teller (BET) specific surface areas of the samples were detected by Micromeritics Tristar 3000 instrument. Photoluminescence (PL) spectra were collected using the Horiba Fluorolog-3 instrument, and the wavelength of the exciting light was 400 nm.

2.3 Synthesis of the samples

2.3.1 Synthesis of 3D-STO

The 3D-STO material was synthesized via a colloidal crystal template (CCT) method according to our previous report [22]. Polymethyl methacrylate (PMMA) microspheres with an average particle size of 300 nm were used. In the experiment, tetrabutyl titanate (0.01 mol) and acetic acid (10 mL) were added to a beaker. Then, deionized water (10 mL) was added dropwise with magnetic stirring. Afterward, a 10 mL aqueous solution containing 0.01 mol lanthanum nitrate and 10 mL citric acid solution ($2\ mol \cdot L^{-1}$) was sequentially added dropwise to the beaker. The resulting solution was stirred at room temperature for another 30 min, and then a clear solution was obtained. Then, the PMMA CCT was soaked in the abovementioned precursor solution for about 3 h and collected by filtration to remove excess precursor solution. After vacuum drying at 50 °C overnight, the samples were heated in a muffle furnace to 650 °C with a heating rate of 1 $°C \cdot min^{-1}$ and calcined for 4 h. The obtained material was labeled 3D-STO. For comparison, a $SrTiO_3$ material with a disordered porous structure was prepared through a process similar to that of 3D-STO, except that the CCT was replaced by a disordered polymer microsphere template. The obtained sample was labeled Disorder-STO.

2.3.2 Synthesis of $Zn_xCd_{1-x}S$ solid solution materials

The $Zn_xCd_{1-x}S$ solid solution nanoparticles were prepared through a chemical co-precipitation method in the presence of α-monothioglycerol according to the literature [37]. For the synthesis of $Zn_{0.5}Cd_{0.5}S$, the solution of cadmium acetate (10 mL, 0.5 mol·L^{-1}), zinc acetate (10 mL, 0.5 mol·L^{-1}), sodium sulfide (20 mL, 0.5 mol·L^{-1}) and 20 mL α-monothioglycerol were added into a round bottom flask. The reaction was performed at 80 °C for 3 h under magnetic stirring. After cooling to room temperature, the orange precipitate was centrifuged and then washed with deionized water and ethanol several times. The samples were dried in a vacuum at 50 °C for 9 h. By tuning the molar ratio of Zn/Cd in the synthesis process, a series of $Zn_xCd_{1-x}S$ (x = 0, 0.15, 0.25, 0.5, 0.75, 0.85, 1) solid solution materials were obtained. For simplicity, the $Zn_{0.5}Cd_{0.5}S$ was labeled ZCS.

2.3.3 Synthesis of ZCS-modified 3D-STO

3D-STO (100 mg) and different amounts of ZCS (10, 25, 50, 75, and 100 mg) were dispersed in 35 mL deionized water under magnetic stirring for 4 h. Then, the solid powders were collected by centrifugation and dried under vacuum at 50 °C for 9 h. The obtained ZCS-modified 3D-STO photocatalyst was labeled SZy, where y represents the mass ratio of ZCS in the composites.

2.4 Photocatalytic hydrogen evolution reactions

The hydrogen evolution reactions were performed in a 150 mL quartz reactor with a continuous state of vacuum under visible light irradiation ($\lambda > 420$ nm). Typically, the photocatalyst (25 mg) and 50 mL deionized water containing Na_2SO_3 (0.1 mol·L^{-1}) and Na_2S (0.1 mol·L^{-1}) were added into the quartz reactor. A certain amount of chloroplatinic acid aqueous solution was used as the precursor of Pt co-catalyst through an *in situ* photo-deposition method. Then, the reactor was irradiated by a 300 W Xe lamp with an ultraviolet cut-off filter ($\lambda > 420$ nm) under magnetic stirring and degassing conditions. Online gas chromatograph was used to real-time monitor the hydrogen evolution rate in real time.

2.5 Photoelectrochemical measurements

The obtained photocatalyst (2 mg) was dispersed into a 1 mL mixed solution made up of ethanol and Nafion® 117 with a volume ratio of 100:1. After ultrasonic treatment for 10 min, the supernatant of the mixture was dropped onto the fluorine-doped tin oxide (FTO) glass with an area of 1.0 cm × 1.0 cm and the obtained electrode was dried overnight at room temperature. The FTO glass containing the sample acted as the working electrode, Pt plate acted as the counter electrode, and Ag/AgCl (saturated KCl) was the reference electrode. A 0.1 mol·L^{-1} Na_2SO_4 aqueous solution was used as the electrolyte. The electrochemical impedance spectroscopy (EIS) and Mott-Schottky (M-S) measurements were performed on an electrochemical workstation (CHI 760D) using a conventional three-electrode cell. Besides, the open-circuit voltage of the photocurrent-time was fixed at 0.36 V and the light source was supplied by a 300W Xe lamp with a 420 nm ultraviolet cut-off filter. The alternating current signal was set to a frequency of 1 kHz in the M-S tests.

3 Results and discussion

3.1 Characterization of the samples

The XRD patterns of as-synthesized samples are shown in Fig. 1. From Fig. 1(a), the characteristic diffraction peaks of pure CdS and ZnS were identified as cubic sphalerite phase (JCPDF No. 05-0566) and cubic hawleyite structure

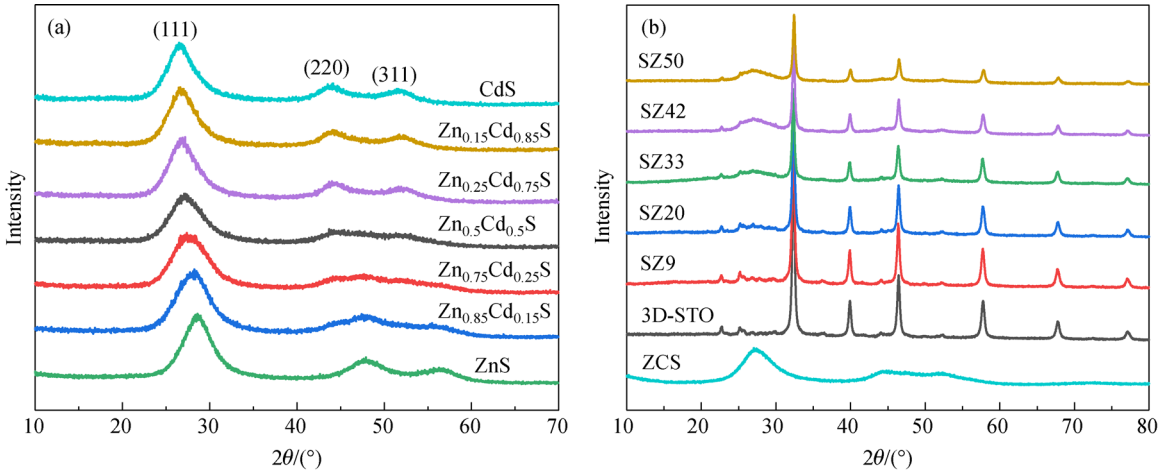

Fig. 1 Powder XRD patterns of the as-synthesized (a) $Zn_xCd_{1-x}S$ solid solutions and (b) SZy composites.

(JCPDF No. 10-0454), respectively. Meanwhile, with the increase in Zn molar ratio in $Zn_xCd_{1-x}S$, the diffraction peaks shifted to a larger diffraction angle direction due to the smaller lattice parameter of ZnS compared with CdS. No obvious peak broadening or splitting was observed, indicating the successful synthesis of $Zn_xCd_{1-x}S$ solid solution materials. Figure 1(b) shows the powder XRD patterns of the obtained SZ*y* photocatalysts. The characteristic diffraction peaks of 3D-STO could be indexed to a typical cubic perovskite phase (JCPDS No.35-0734). With the increase in the loading amount of ZCS, the (111) peak intensity of $Zn_xCd_{1-x}S$ gradually increased. No other peaks related to impurities were observed from these XRD patterns, suggesting the successful synthesis of SZ*y* photocatalysts.

Figure 2 shows the SEM images of the obtained SZ*y* photocatalysts. As shown in Fig. 2(a), a well-ordered inverse opal structure of pure 3D-STO was observed. The diameter of the macropores was 185 nm. From Figs. 2(b–f), the ZCS nanoparticles were decorated into the macropores of 3D-STO. With the increase in ZCS loading amount, the macropores of 3D-STO were gradually filled. However, the well-ordered inverse opal structure of 3D-STO was maintained on these SZ*y* composites. As for SZ50, the surfaces of 3D-STO were nearly completely covered by ZCS (Fig. 2(f)). The SEM-EDS elemental mapping images of SZ33 are shown in Fig. S1 (cf. Electronic Supplementary Material, ESM). Six elements, including Sr, Ti, O, Zn, Cd, and S, were evenly dispersed in SZ33, suggesting the uniform dispersion of ZCS on the surface of 3D-STO. The SEM images of Disorder-SZ33 are shown in Fig. S2 (cf. ESM). Some ZCS nanoparticles were decorated on the surface of Disorder-STO with a disordered macroporous structure.

The TEM and high-resolution TEM (HRTEM) images of SZ33 are shown in Fig. 3. The ZCS nanoparticles with a particle size of 10–50 nm (as shown in Fig. S3 (cf. ESM)) dispersed onto the macropores of 3D-STO. The marked lattice spacings of 0.27 and 0.32 nm corresponded to the (110) plane of 3D-STO and (111) plane of ZCS, respectively. As shown in Fig. S4 (cf. ESM), the Ti, Sr, and O elements were evenly dispersed in SZ33 and some ZCS nanoparticles decorated on the surface of 3D-STO. The BET specific surface areas and Barrett-Joyner-Halenda (BJH) pore volumes of the samples were detected. The results are listed in Table 1. The BET surface areas of 3D-STO and ZCS were 44.4 and 154.4 $m^2 \cdot g^{-1}$, respectively. The larger BET surface area of ZCS could be attributed to its smaller particle size. For SZ*y* composites, with the increase in ZCS loading amount, their surface areas gradually increased from 45.8 to 104.1 $m^2 \cdot g^{-1}$. However, the composite photocatalysts exhibited increased BJH pore volumes compared with pure 3D-STO and ZCS, which could be attributed to the aggregation of ZCS nanoparticles in the macropores of 3D-STO, resulting in the formation of accumulated mesoporous structure.

Figure 4 presents the DR UV-Vis spectra and the $(\alpha h\nu)^2$-$h\nu$ plots of the samples. As shown in Fig. 4(a), pure 3D-STO only absorbed ultraviolet light with a wavelength below 380 nm, whereas ZCS exhibited an obvious absorbance in the visible light region starting from 700 nm. The optical absorption edges of SZ*y* composites were redshifted to approximately 560 nm compared with 3D-STO. Moreover, with the increase in ZCS loading amount, the light absorption ability of SZ*y* in the visible light region gradually enhanced. The DR UV-Vis spectrum of Disorder-SZ33 is shown in Fig. S5 (cf. ESM). A very similar light absorption curve with SZ33 appeared. Through a transform of DR UV-Vis spectra using the Kubelka–Munk function, the plots of $(\alpha h\nu)^2$-$h\nu$ of 3D-STO and ZCS were obtained (Fig. 4(b)) [38,39]. The bandgaps of 3D-STO and ZCS were determined as approximately 3.27 and 2.20 eV, respectively.

The surface composition and chemical states of SZ33

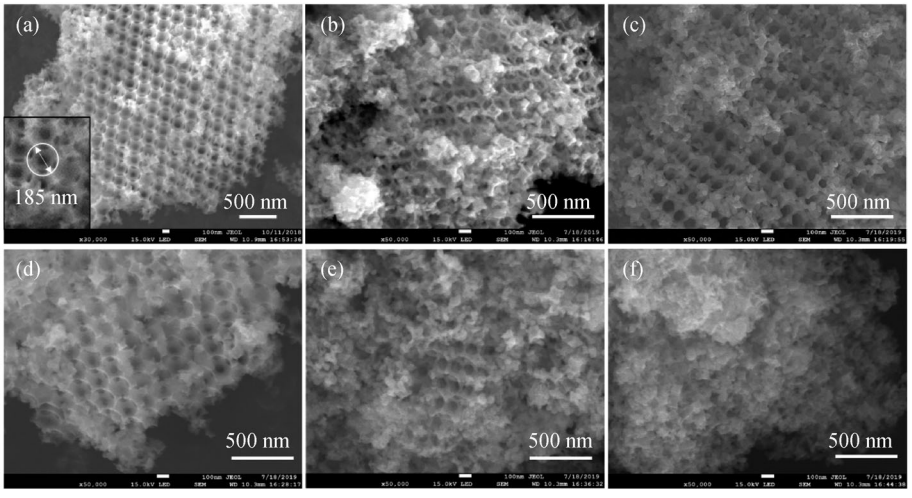

Fig. 2 SEM images of (a) 3D-STO, (b) SZ9, (c) SZ20, (d) SZ33, (e) SZ42, and (f) SZ50.

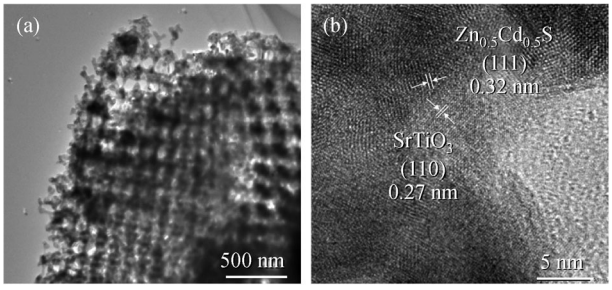

Fig. 3 (a) TEM and (b) HRTEM images of SZ33.

Table 1 Specific surface areas and pore volumes of the samples

Sample	BET surface area/($m^2 \cdot g^{-1}$)	BJH pore volume/($cm^3 \cdot g^{-1}$)
3D-STO	44.4	0.164
SZ9	45.8	0.189
SZ20	57.1	0.190
SZ33	86.6	0.193
SZ42	135.9	0.305
SZ50	104.1	0.226
ZCS	154.4	0.091

and its single counterparts were determined by XPS characterization. The results are shown in Figs. 5, S6 (cf. ESM), and S7 (cf. ESM). The Ti 2p XPS spectrum exhibited two signals of Ti $2p_{3/2}$ and Ti $2p_{1/2}$ with the binding energies of 458.2 and 464.0 eV, respectively (Fig. 5(a)), which could be ascribed to Ti^{4+}. The Sr 3d XPS spectrum (Fig. 5(b)) showed two peaks at 132.6 and 134.4 eV, corresponding to the characteristic binding energies of Sr $3d_{5/2}$ and $3d_{3/2}$ of Sr^{2+}, respectively. The Cd 3d XPS spectrum (Fig. 5(c)) exhibited two peaks at the binding energies of 404.6 and 411.3 eV, corresponding to Cd $3d_{5/2}$ and $3d_{3/2}$ of Cd^{2+}, respectively [40]. Figure 5(d) showed that two peaks of Zn $2p_{3/2}$ and Zn $2p_{1/2}$ were discerned at 1021.9 and 1044.5 eV, which were the typical values of Zn^{2+}. As depicted in Fig. 5(e), the O 1s XPS spectrum revealed several components. The peak at 529.6 eV corresponded to the lattice stoichiometric oxygen in STO, whereas the peak at 531.6 eV could be assigned to the chemisorbed oxygen species, which could be related to the surface defective oxygen [41]. The S 2p XPS spectrum of SZ33 (Fig. 5(f)) can be deconvoluted into three peaks with binding energies at 161.2, 162.7, and 164.1 eV. The peaks located at 161.2 and 162.7 eV could be, respectively, ascribed to the S $2p_{3/2}$ and $2p_{1/2}$ peaks of S^{2-} [42], which can also be observed in the S 2p XPS spectrum of pure ZCS (Fig. S5(c)). Notably, a new peak at 164.1 eV appeared in the S 2p XPS spectrum of SZ33 but not pure ZCS. It could be assigned to the formation of an interfacial metal–sulfur bond (e.g., Ti–S bond) [43], which should facilitate charge transfer through the interface.

3.2 Photocatalytic hydrogen evolution reactions

The obtained photocatalysts were evaluated in photocatalytic hydrogen evolution reactions under visible light irradiation ($\lambda > 420$ nm), and the results are shown in Fig. 6. As shown in Fig. 6(a), $Zn_xCd_{1-x}S$ solid solutions exhibited obviously enhanced photocatalytic activity compared with pure ZnS and CdS. Among the $Zn_xCd_{1-x}S$ samples, ZCS showed the highest hydrogen evolution rate (4.67 $mmol \cdot g^{-1} \cdot h^{-1}$), which was 8.1 times as high as that of pure CdS (0.58 $mmol \cdot g^{-1} \cdot h^{-1}$). Therefore, ZCS was selected for further investigation.

From Fig. 6(b), SZ33, SZ42, and SZ50 exhibited improved hydrogen evolution rates compared with pure ZCS. 3D-STO exhibited a negligible hydrogen evolution rate under visible light irradiation due to its large bandgap. In particular, among the SZ*y* samples, SZ33 showed the highest hydrogen evolution rate (19.7 $mmol \cdot g^{-1} \cdot h^{-1}$), which was 4.2 times higher than that of pure ZCS. Moreover, compared with similar S-based semiconductor photocatalysts reported in the literature (as listed in Table

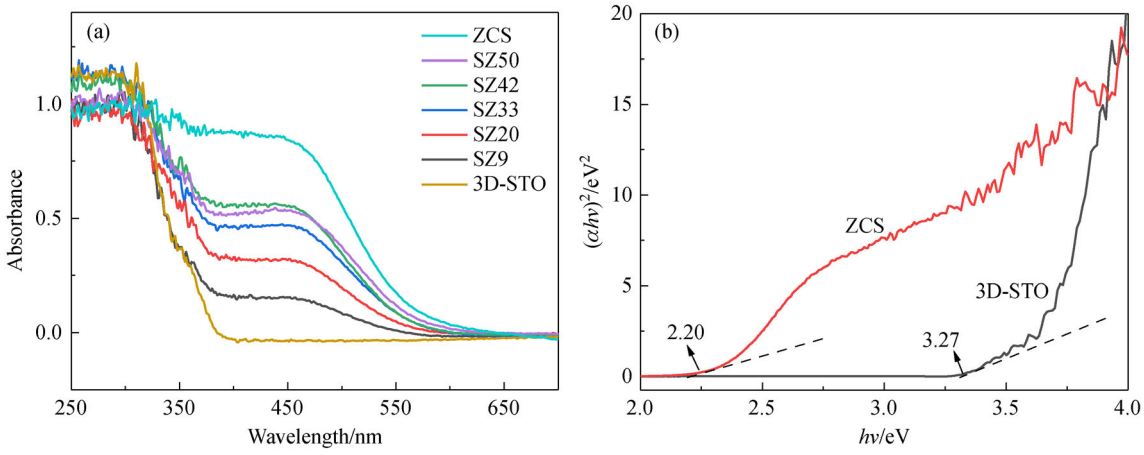

Fig. 4 (a) DR UV-Vis spectra of 3D-STO, ZCS and SZ*y*; (b) $(\alpha h\nu)^2$-$h\nu$ plots of 3D-STO and ZCS.

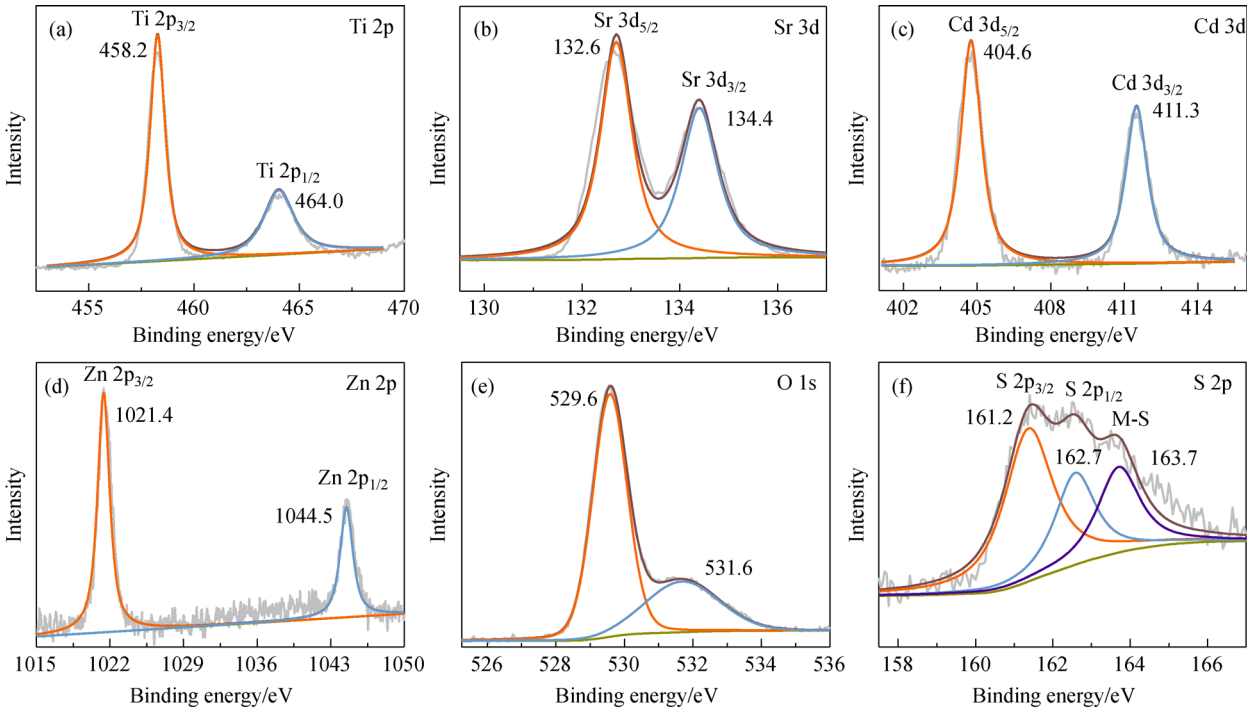

Fig. 5 High-resolution XPS spectra of (a) Ti 2p, (b) Sr 3d, (c) Cd 3d, (d) Zn 2p, (e) O 1s, and (f) S 2p of SZ33.

S1, cf. ESM), SZ33 still exhibited significantly enhanced performance in hydrogen evolution reactions. SZ9 and SZ20 exhibited lower activity than pure ZCS, which could be attributed to the lower contents of ZCS with visible light responsibility. However, SZ42 and SZ50 with higher loading amount of ZCS exhibited lower activity than SZ33 because more ZCS nanoparticles filled up the macropores of 3D-STO, which not only decreased the efficiency of interfacial charge transfer but also affected the slow photon effect of 3D-STO.

Figure 6(c) shows the photocatalytic hydrogen evolution rates of SZ33 with different Pt loading amounts. The highest hydrogen evolution rate can be achieved when 1.5 wt-% Pt was *in situ* photo-deposited as co-catalyst. The hydrogen evolution performance of SZ33 would be suppressed under a low or high loading amount of Pt co-catalyst, which could be explained by the reduced proton reduction active sites or the increased particle size of co-catalysts. Remarkably, even under Pt-free conditions, SZ33 still exhibited a promising hydrogen evolution rate (3.23 $mmol \cdot g^{-1} \cdot h^{-1}$), which was close to the performance of pure ZCS using 1.5 wt-% Pt as co-catalysts, and much higher than that of pure CdS with 1.5 wt-% Pt. Therefore, SZ33 should be a promising candidate for noble metal-free photocatalysts in hydrogen evolution reaction under visible light irradiation. To properly evaluate the efficiency of the obtained photocatalysts, the apparent quantum efficiency value of SZ33 for hydrogen evolution was measured according to the reported method [44] under 420 nm wavelength light irradiation, and the calculated value was 35.9%.

To further confirm the slow photon effect of the SZ*y* composites, the catalytic activity of SZ33 was compared with that of Disorder-SZ33, which was synthesized using Disorder-STO and ZCS. As shown in Fig. 6(d), SZ33 exhibited higher performance than Disorder-SZ33 (9.45 $mmol \cdot g^{-1} \cdot h^{-1}$). The hydrogen evolution rate of SZ33 was two times than that of Disorder-SZ33, confirming the contribution of the slow photon effect of 3D-STO.

The stability of SZ*y* composite photocatalysts was evaluated by a cycling experiment as shown in Fig. 7. From Fig. 7(a), after five photocatalytic experiment cycles, the hydrogen evolution rate of SZ33 attained 16.3 $mmol \cdot g^{-1} \cdot h^{-1}$. Only a slight decrease of activity was observed, which might be attributed to the consumption of sacrifice reagents and the partial photocorrosion of some exposed ZCS [45]. In addition, no obvious changes can be observed from the XRD patterns of fresh and used SZ33 samples (Fig. 7(b)), indicating that the obtained composite photocatalysts were quite stable.

3.3 Promoting mechanism of photocatalysts

According to the discussion in the above section, the slow photon effect of 3D-STO was crucial in promoting the photocatalytic activity of SZy composites. Thus, the photonic stop-band of 3D-STO used in the experiments was calculated through modified Bragg's law (Eq. (1)) [46,47]:

$$\lambda_{max} = 2\sqrt{\frac{2}{3}}D\sqrt{n^2_{SrTiO_3}f + n^2_{water}(1-f) - \sin^2\theta}, \quad (1)$$

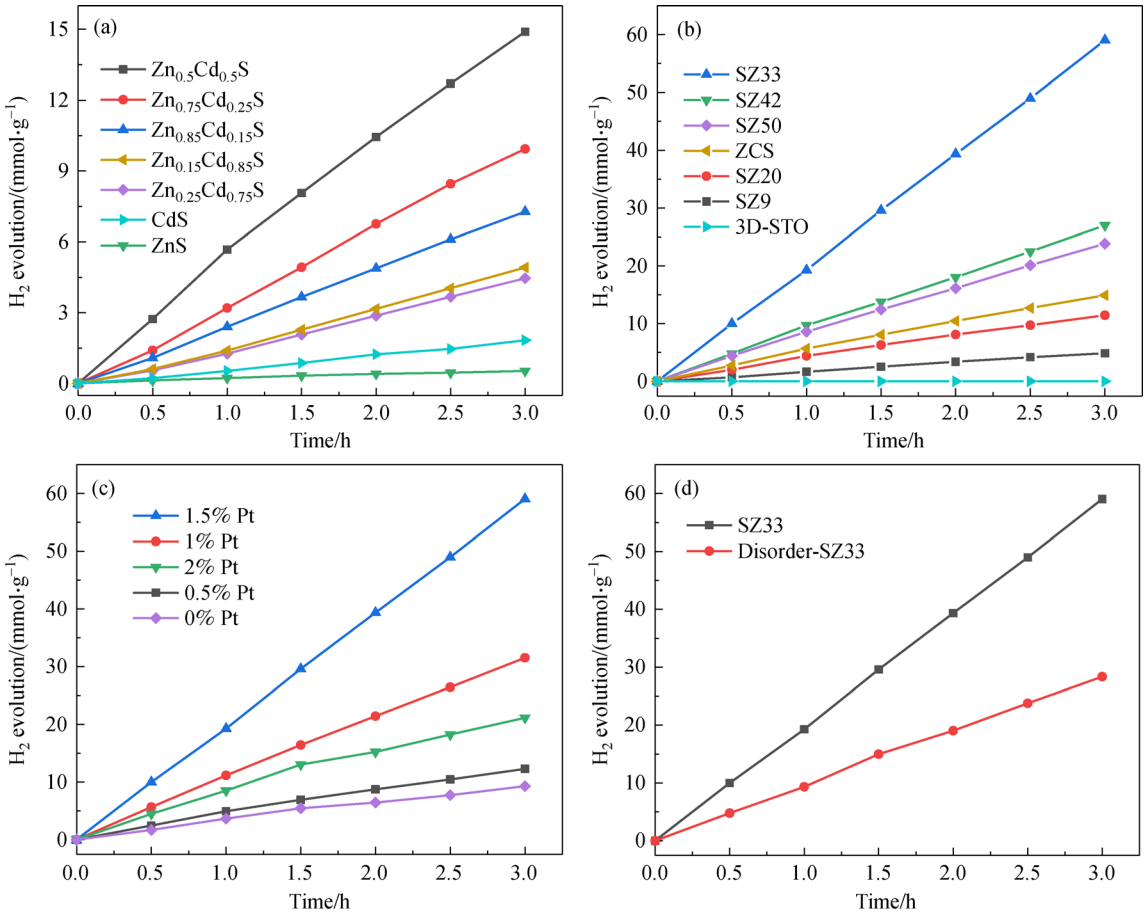

Fig. 6 Photocatalytic hydrogen evolution rates under visible light irradiation ($\lambda > 420$ nm) catalyzed by (a) $Zn_xCd_{1-x}S$ and (b) SZ*y* loading 1.5 wt-% Pt as co-catalyst, and (c) SZ33 with different Pt loading amount; (d) photocatalytic hydrogen evolution rates under visible light irradiation ($\lambda > 420$ nm) on SZ33 and Disorder-SZ33.

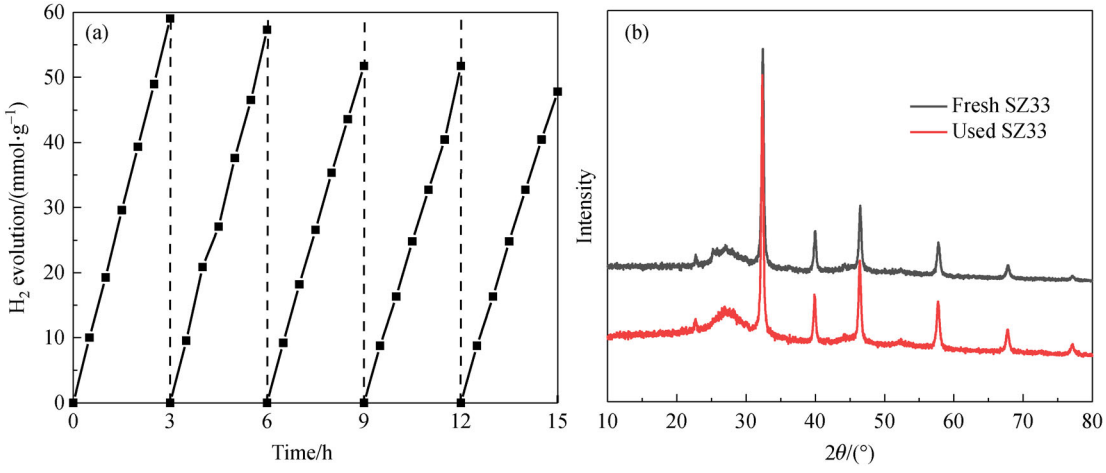

Fig. 7 (a) Cycling experiments of SZ33 in photocatalytic hydrogen evolution under visible light irradiation ($\lambda > 420$ nm); (b) powder XRD patterns of fresh and used SZ33.

where λ_{max} is the wavelength of the photonic bandgap, D is the diameter of macropores ($D = 185$ nm in this study), n is the refractive index of the substrate, f is the volume fraction of 3D-STO (usually given as 0.26), and θ is the incident angle of light. For normal incidence ($\theta = 0°$), the calculated photonic stop-band was 507 nm, meaning that the incident

light with a wavelength of 507 nm should be completely reflected. For the suspended photocatalysts, the multiple reflections of incident light should increase the photon absorption probability. As for the incident lights with the wavelength at the blue [48] and red edges [10] of the stop-band, their group velocity should be significantly suppressed and the photon-matter interaction should be enhanced. For SZ33, from Fig. 4(a), the effective light absorption range of SZ33 was located in the range of 420–570 nm, which exactly overlapped with the blue and red edges of the stop-band of 3D-STO. Therefore, it can be concluded that the slow photon effect of 3D-STO played a crucial role in promoting the light-harvesting efficiency of photocatalysts.

To investigate the charge transfer and separation efficiency of SZ*y* photocatalysts, PL spectra and EIS Nyquist plots of the samples were recorded, and the results are shown in Fig. 8. Figure 8(a) shows the PL spectra of 3D-STO, ZCS, and SZ33. The emission intensity of SZ33 was lower than that of 3D-STO and ZCS, indicating the improved separation efficiency of electrons and holes in the SZ33 composite. Figure 8(b) shows the EIS Nyquist plots of the samples. SZ33 exhibited a smaller semicircle diameter than 3D-STO and ZCS, suggesting the smaller equivalent resistance of the charge transfer at the electrode interface. The results of PL spectra and EIS Nyquist plots indicated that the composite photocatalyst exhibited enhanced charge migration and separation efficiency compared with their single counterparts.

To investigate the charge transfer mechanism of obtained composite photocatalysts, the electronic band structure of 3D-STO and ZCS was determined using M-S tests and measured bandgap energies (Fig. 9). From Fig. 9(a), the slopes of the M-S curves of the 3D-STO and ZCS were positive, indicating that they are *n*-type semiconductors. The point that the tangent line of an M-S curve intersects the X-axis is the flat band potential of the sample. For *n*-type semiconductors, the flat band potential

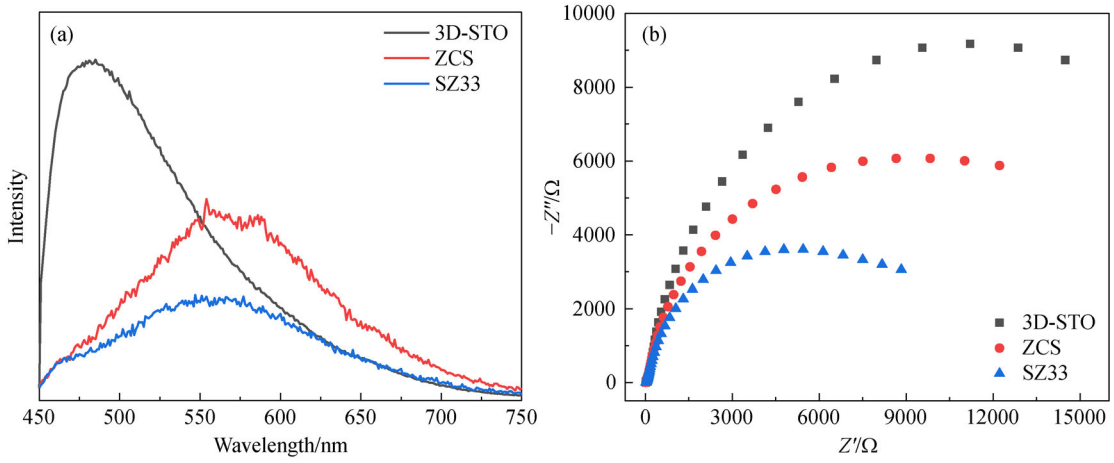

Fig. 8 (a) PL spectra and (b) EIS Nyquist plots of 3D-STO, ZCS and SZ33.

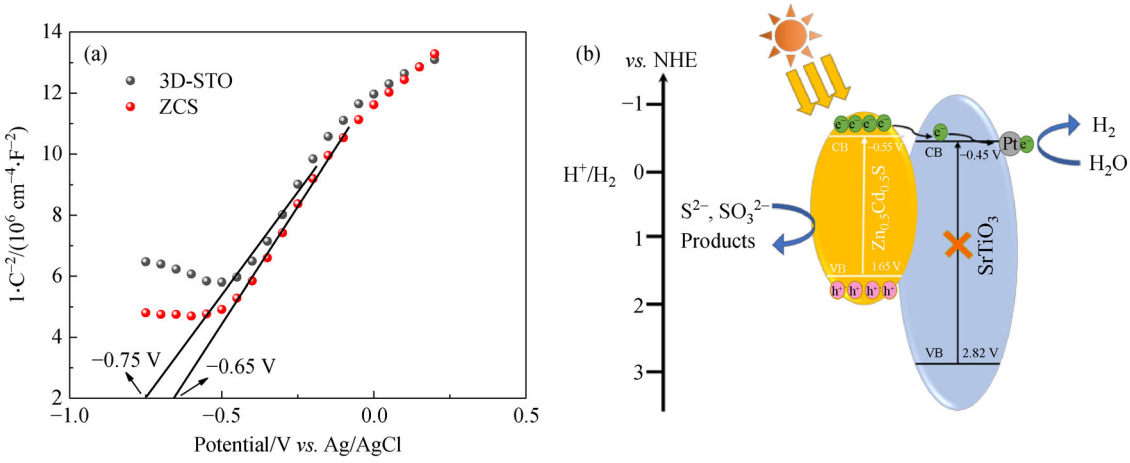

Fig. 9 (a) M-S measurements in 0.1 mol·L^{-1} Na_2SO_4 electrolyte solution of 3D-STO and ZCS samples; (b) schematic diagrams of band structures and proposed charge transfer mechanisms of the composite photocatalysts.

can be approximated as its conduction band (CB) potential. Based on the M-S tests, the CB potentials of 3D-STO and ZCS were determined as –0.65 and –0.75 V (*vs.* Ag/AgCl), respectively. According to E(NHE) = E(Ag/AgCl) + 0.197, their CB potentials can be calculated to be –0.45 and –0.55 V (vs. NHE), respectively. From Fig. 4(b), the bandgaps of 3D-STO and ZCS were 3.27 and 2.20 eV, respectively. Thus, their valence band potentials can be determined as 2.78 V and 1.63 V (*vs.* NHE) for 3D-STO and ZCS, respectively. Based on these results, the electronic band structure of the composite photocatalysts can be described in Fig. 9(b). The electrons in the ZCS will be separated from the holes under visible light irradiation. As the CB potential of 3D-STO was higher than that of ZCS, the electrons in the ZCS will migrate to 3D-STO, resulting in the separation of photogenerated electrons and holes. Therefore, the hydrogen evolution reaction occurred on the CB of 3D-STO, and the oxidation reaction occurred on the valence band of ZCS.

4 Conclusions

In summary, a series of $Zn_xCd_{1-x}S$ nanoparticle modified 3D-STO photocatalysts SZ*y* with excellent performance in hydrogen evolution reaction under visible light irradiation were exploited in this study. These composite photocatalysts exhibited multiplied increased hydrogen evolution rates (up to 19.67 $mmol \cdot g^{-1} \cdot h^{-1}$) compared with pure $Zn_xCd_{1-x}S$, 3D-STO, CdS, and reported S-based semiconductor materials. Importantly, SZ33 showed an attractive hydrogen production rate of 3.23 $mmol \cdot g^{-1} \cdot h^{-1}$ in the absence of Pt co-catalysts. The promoted performance of SZ*y* could be attributed to the synergetic effect of the slow photon effect of 3D-STO and the improved migration and separation efficiencies of photogenerated charge carriers. This study provides a convenient method to fabricate highly efficient visible-light-driven photocatalysts for hydrogen evolution reaction, even under noble metal co-catalyst-free conditions.

Acknowledgements This work was supported by the Natural Science Foundation of Tianjin (Grant No. 17JCYBJC22600), Tianjin Development Program for Innovation and Entrepreneurship, and the Fundamental Research Funds for the Central Universities.

Electronic Supplementary Material Supplementary material is available in the online version of this article at https://dx.doi.org/10.1007/s11705-021-2089-z and is accessible for authorized users.

References

1. Hisatomi T, Domen K. Reaction systems for solar hydrogen production via water splitting with particulate semiconductor photocatalysts. Nature Catalysis, 2019, 2(5): 387–399
2. Tong H, Ouyang S, Bi Y, Umezawa N, Oshikiri M, Ye J H. Nano-photocatalytic materials: possibilities and challenges. Advanced Materials, 2012, 24(2): 229–251
3. Cui Y, Zeng Z, Zheng J, Huang Z, Yang J. Efficient photodegradation of phenol assisted by persulfate under visible light irradiation via a nitrogen-doped titanium-carbon composite. Frontiers of Chemical Science and Engineering, 2021, (in press)
4. Chen S, Qi Y, Li C, Domen K, Zhang F. Surface strategies for particulate photocatalysts toward artificial photosynthesis. Joule, 2018, 2(11): 2260–2288
5. Yang J, Liu X, Cao H, Shi Y, Xie Y, Xiao J. Dendritic $BiVO_4$ decorated with MnO_x co-catalyst as an efficient hierarchical catalyst for photocatalytic ozonation. Frontiers of Chemical Science and Engineering, 2019, 13(1): 185–191
6. Kundu S, Patra A. Nanoscale strategies for light harvesting. Chemical Reviews, 2017, 117(2): 712–757
7. Lu J, Lan L, Liu X T, Wang N, Fan X. Plasmonic Au nanoparticles supported on both sides of TiO_2 hollow spheres for maximising photocatalytic activity under visible light. Frontiers of Chemical Science and Engineering, 2019, 13(4): 665–671
8. Yang Y L, Tang Y, Jiang H M, Chen Y M, Wan P Y, Fan M H, Zhang R R, Ullah S, Pan L, Zou J J, et al. 2020 Roadmap on gas-involved photo-and electro-catalysis. Chinese Chemical Letters, 2019, 30(12): 2089–2109
9. Liu J, Zhao H, Wu M, van der Schueren B, Li Y, Deparis O, Ye J, Ozin G A, Hasan T, Su B L. Slow photons for photocatalysis and photovoltaics. Advanced Materials, 2017, 29(17): 1605349
10. Chen J I L, von Freymann G, Choi S Y, Kitaev V, Ozin G A. Amplified photochemistry with slow photons. Advanced Materials, 2006, 18(14): 1915–1919
11. Arandiyan H, Wang Y, Sun H, Rezaei M, Dai H. Ordered meso- and macroporous perovskite oxide catalysts for emerging applications. Chemical Communications, 2018, 54(50): 6484–6502
12. Chen X, Ye J, Ouyang S, Kako T, Li Z, Zou Z. Enhanced incident photon-to-electron conversion efficiency of tungsten trioxide photoanodes based on 3D-photonic crystal design. ACS Nano, 2011, 5(6): 4310–4318
13. Chang Y, Yu K, Zhang C, Li R, Zhao P, Lou L L, Liu S. Three-dimensionally ordered macroporous WO_3 supported Ag_3PO_4 with enhanced photocatalytic activity and durability. Applied Catalysis B: Environmental, 2015, 176: 363–373
14. Chang Y, Xuan Y, Quan H, Zhang H, Liu S, Li Z, Yu K, Cao J. Hydrogen treated Au/3DOM-TiO_2 with promoted photocatalytic efficiency for hydrogen evolution from water splitting. Chemical Engineering Journal, 2020, 382: 122869
15. Zalfani M, Van Der Schueren B, Hu Z, Rooke J C, Bourguiga R, Wu M, Li Y, Tendeloo G V, Su B L. Novel 3DOM $BiVO_4/TiO_2$ nanocomposites for highly enhanced photocatalytic activity. Journal of Materials Chemistry. A, Materials for Energy and Sustainability, 2015, 3(42): 21244–21256
16. Lin B, Li J, Xu B, Yan X, Yang B, Wei J, Yang G. Spatial positioning effect of dual cocatalysts accelerating charge transfer in three dimensionally ordered macroporous g-C_3N_4 for photocatalytic hydrogen evolution. Applied Catalysis B: Environmental, 2019, 243: 94–105
17. Ji K, Dai H, Deng J, Zang H, Arandiyan H, Xie S, Yang H. 3DOM $BiVO_4$ supported silver bromide and noble metals: high-performance photocatalysts for the visible-light-driven degradation of 4-

chlorophenol. Applied Catalysis B: Environmental, 2015, 168: 274–282

18. Ji K, Deng J, Zang H, Han J, Arandiyan H, Dai H. Fabrication and high photocatalytic performance of noble metal nanoparticles supported on 3DOM $InVO_4$-$BiVO_4$ for the visible-light-driven degradation of rhodamine B and methylene blue. Applied Catalysis B: Environmental, 2015, 165: 285–295
19. Song Y, Li N, Chen D, Xu Q, Li H, He J, Lu J. 3D ordered MoP inverse opals deposited with CdS quantum dots for enhanced visible light photocatalytic activity. Applied Catalysis B: Environmental, 2018, 238: 255–262
20. Zhang C, Zhao P, Liu S, Yu K. Three-dimensionally ordered macroporous perovskite materials for environmental applications. Chinese Journal of Catalysis, 2019, 40(9): 1324–1338
21. Zhang G, Liu G, Wang L, Irvine J T S. Inorganic perovskite photocatalysts for solar energy utilization. Chemical Society Reviews, 2016, 45(21): 5951–5984
22. Yu K, Zhang C, Chang Y, Feng Y, Yang Z, Yang T, Lou L L, Liu S. Novel three-dimensionally ordered macroporous $SrTiO_3$ photocatalysts with remarkably enhanced hydrogen production performance. Applied Catalysis B: Environmental, 2017, 200: 514–520
23. Chang Y, Yu K, Zhang C, Yang Z, Feng Y, Hao H, Jiang Y, Lou L L, Zhou W, Liu S. Ternary CdS/Au/3DOM-$SrTiO_3$ composites with synergistic enhancement for hydrogen production from visible-light photocatalytic water splitting. Applied Catalysis B: Environmental, 2017, 215: 74–84
24. Wu X, Wang C, Wei Y, Xiong J, Zhao Y, Zhao Z, Liu J, Li J. Multifunctional photocatalysts of Pt-decorated 3DOM perovskite-type $SrTiO_3$ with enhanced CO_2 adsorption and photoelectron enrichment for selective CO_2 reduction with H_2O to CH_4. Journal of Catalysis, 2019, 377: 309–321
25. Zhang C, Yu K, Feng Y, Chang Y, Yang T, Xuan Y, Lei D, Lou L L, Liu S. Novel 3DOM-$SrTiO_3$/Ag/Ag_3PO_4 ternary Z-scheme photocatalysts with remarkably improved activity and durability for contaminant degradation. Applied Catalysis B: Environmental, 2017, 210: 77–87
26. Cheng L, Xiang Q, Liao Y, Zhang H. CdS-based photocatalysts. Energy & Environmental Science, 2018, 11(6): 1362–1391
27. Wang F, Kan Z G, Cao F, Guo Q, Xu Y L, Qi C Y, Li C L. Synergistic effects of CdS in sodium titanate based nanostructures for hydrogen evolution. Chinese Chemical Letters, 2018, 29(9): 1417–1420
28. Zhang D P, Wang P F, Chen F Y, Mu K L, Li Y, Wang H T, Ren Z J, Zhan S H. *In situ* integration of efficient photocatalyst $Cu_{1.8}S$/$Zn_xCd_{1-x}S$ heterojunction derived from a metal-organic framework. Chinese Chemical Letters, 2020, 31(10): 2795–2798
29. Li H, Chen Z H, Zhao L, Yang G D. Synthesis of TiO_2@$ZnIn_2S_4$ hollow nanospheres with enhanced photocatalytic hydrogen evolution. Rare Metals, 2019, 38(5): 420–427
30. Li Q, Meng H, Zhou P, Zheng Y, Wang J, Yu J, Gong J. $Zn_{1-x}Cd_xS$ solid solutions with controlled bandgap and enhanced visible-light photocatalytic H_2-production activity. ACS Catalysis, 2013, 3(5): 882–889
31. Zhong J, Zhang Y, Hu C, Hou R, Yin H, Li H, Huo Y. Supercritical solvothermal preparation of a $Zn_xCd_{1-x}S$ visible photocatalyst with enhanced activity. Journal of Materials Chemistry. A, Materials for Energy and Sustainability, 2014, 2(46): 19641–19647
32. Zhu X, Yu S, Gong X, Xue C. *In situ* decoration of $Zn_xCd_{1-x}S$ with FeP for efficient photocatalytic generation of hydrogen under irradiation with visible light. ChemPlusChem, 2018, 83(9): 825–830
33. Dai D, Xu H, Ge L, Han C, Gao Y, Li S, Lu Y. *In situ* synthesis of CoP co-catalyst decorated $Zn_{0.5}Cd_{0.5}S$ photocatalysts with enhanced photocatalytic hydrogen production activity under visible light irradiation. Applied Catalysis B: Environmental, 2017, 217: 429–436
34. Zhang X, Zhao Z, Zhang W, Zhang G, Qu D, Miao X, Sun S, Sun Z. Surface defects enhanced visible light photocatalytic H_2 production for Zn-Cd-S solid solution. Small, 2016, 12(6): 793–801
35. Zhao X, Feng J, Liu J, Shi W, Yang G, Wang G C, Cheng P. An efficient, visible-light-driven, hydrogen evolution catalyst NiS/$Zn_xCd_{1-x}S$ nanocrystal derived from a metal-organic framework. Angewandte Chemie International Edition, 2018, 130(31): 9938–9942
36. Xue C, Li H, An H, Yang B, Wei J, Yang G. NiS_x quantum dots accelerate electron transfer in $Cd_{0.8}Zn_{0.2}S$ photocatalytic system via an rGO nanosheet "Bridge" toward visible-light-driven hydrogen evolution. ACS Catalysis, 2018, 8(2): 1532–1545
37. Sharma M, Singh S, Pandey O P. Excitation induced tunable emission in biocompatible chitosan capped ZnS nanophosphors. Journal of Applied Physics, 2010, 107(10): 104319
38. Zhao H, Liu H, Sun R, Chen Y, Li X A. $Zn_{0.5}Cd_{0.5}S$ photocatalyst modified by 2D black phosphorus for efficient hydrogen evolution from water. ChemCatChem, 2018, 10(19): 4395–4405
39. Xuan Y, Quan H, Shen Z, Zhang C, Yang X, Lou L L, Liu S, Yu K. Band-gap and charge transfer engineering in red phosphorus-based composites for enhanced visible-light-driven H_2 evolution. Chemistry (Weinheim an der Bergstrasse, Germany), 2020, 26(10): 2285–2292
40. Ning X, Zhen W, Wu Y, Lu G. Inhibition of CdS photocorrosion by Al_2O_3 shell for highly stable photocatalytic overall water splitting under visible light irradiation. Applied Catalysis B: Environmental, 2018, 226: 373–383
41. Yu K, Lei D, Feng Y, Yu H, Chang Y, Wang Y, Liu Y, Wang G C, Lou L L, Liu S, Zhou W. The role of Bi-doping in promoting electron transfer and catalytic performance of Pt/3DOM-$Ce_{1-x}Bi_xO_{2-\delta}$. Journal of Catalysis, 2018, 365: 292–302
42. Chang Y, Xuan Y, Zhang C, Hao H, Yu K, Liu S. Z-Scheme Pt@CdS/3DOM-$SrTiO_3$ composite with enhanced photocatalytic hydrogen evolution from water splitting. Catalysis Today, 2019, 327: 315–322
43. Li B, Tian Z, Li H, Yang Z, Wang Y, Wang X. Self-supporting graphene aerogel electrode intensified by $NiCo_2S_4$ nanoparticles for asymmetric supercapacitor. Electrochimica Acta, 2019, 314: 32–39
44. Wang Z, Hisatomi T, Li R, Sayama K, Liu G, Domen K, Li C, Wang L. Efficiency accreditation and testing protocols for particulate photocatalysts toward solar fuel production. Joule, 2021, 5(2): 344–359
45. Yu T, Lv Z, Wang K, Sun K, Liu X, Wang G, Jiang L, Xie G. Constructing $SrTiO_3$-T/CdZnS heterostructure with tunable oxygen vacancies for solar-light-driven photocatalytic hydrogen evolution. Journal of Power Sources, 2019, 438: 227014
46. Ren M, Ravikrishna R, Valsaraj K T. Photocatalytic degradation of

gaseous organic species on photonic band-gap titania. Environmental Science & Technology, 2006, 40(22): 7029–7033

47. Zhang K, Liu Y, Deng J, Xie S, Lin H, Zhao X, Yang J, Han Z, Dai H. Fe_2O_3/3DOM $BiVO_4$: high-performance photocatalysts for the visible light-driven degradation of 4-nitrophenol. Applied Catalysis B: Environmental, 2017, 202: 569–579
48. Zhao H, Hu Z, Liu J, Li Y, Wu M, Van Tendeloo G, Su B L. Blue-edge slow photons promoting visible-light hydrogen production on gradient ternary 3DOM TiO_2-Au-CdS photonic crystals. Nano Energy, 2018, 47: 266–274